metals

Article

Multi-Component Evaporation and Uneven Aluminum Distribution during High-Power Vacuum Laser Welding of Ti-6Al-4V Titanium Alloy

Bingqi Wang [1], Shuaifeng Zhang [2], Xinyue Tan [1], Yifan Lv [2], Lvjie Liang [3], Zhiqian Liao [2,*] and Anguo Huang [1,*]

1 State Key Laboratory of Materials and Die & Mould Technology, Huazhong University of Science and Technology, Wuhan 430074, China
2 Luoyang Ship Material Research Institute, Luoyang 471023, China
3 School of Mechanical & Electrical Engineering, Wuhan Institute of Technology, Wuhan 430074, China
* Correspondence: zhsf_9312@stu.xjtu.edu.cn (Z.L.); huang-anguo@hust.edu.cn (A.H.); Tel.: +86-027-875-436-76 (A.H.)

Abstract: Titanium alloy is an important material for the manufacture of key components of deep-sea submersibles. High-power vacuum laser welding is an important method for welding TC4 thick plate (40–120 mm) structures. However, due to the low melting point of aluminum, its uneven distribution in the weld caused by evaporation during welding affects the quality of joints. This paper conducted experimental and simulation studies to investigate the effect of process parameters on multi-component evaporation and uneven aluminum distribution. Based on a three-dimensional model of vacuum laser welding, the mechanism of the uneven distribution of aluminum in the weld is explained. The results show that the uneven distribution of aluminum in the weld is mainly related to the metal vapor behavior and keyhole morphology. As the welding speed rises from 1 m/min to 3 m/min, the proportion of aluminum in the metal vapor and the degree of compositional unevenness increase. When the laser power increases from 6 kW to 18 kW, the proportion of aluminum in the metal vapor and degree of unevenness increase, peak at 12 kW, and then decrease. This work facilitates the selection of suitable process parameters to reduce aluminum evaporation during the high-power vacuum welding of Ti-6Al-4V alloys. Joints with a more stable performance can be obtained by avoiding the uneven distribution of aluminum.

Keywords: Ti-6Al-4V titanium alloy; vacuum laser welding; aluminum evaporation loss; numerical simulation

check for updates

Citation: Wang, B.; Zhang, S.; Tan, X.; Lv, Y.; Liang, L.; Liao, Z.; Huang, A. Multi-Component Evaporation and Uneven Aluminum Distribution during High-Power Vacuum Laser Welding of Ti-6Al-4V Titanium Alloy. *Metals* **2023**, *13*, 1196. https://doi.org/10.3390/met13071196

Academic Editors: Aleksander Lisiecki and Leu-Wen Tsay

Received: 26 April 2023
Revised: 16 June 2023
Accepted: 26 June 2023
Published: 28 June 2023

1. Introduction

As a popular non-ferrous metal material, titanium alloys are widely applied to various fields, such as aerospace [1], beams [2], ships [3], aviation [4], and nuclear power [5]. Especially in the field of deep-sea submarines, titanium alloy thick plate (40–120 mm) is an important material for manufacturing their key components. Due to the increasing use of titanium alloys in large structural parts, the method of obtaining large melt depths at a low cost has attracted attention. Laser welding is commonly used in the welding of titanium alloys due to its high energy density. However, it is becoming difficult to obtain the required penetration depth only by increasing the energy input. Zhu B. et al. researched melt flow rules in laser deep penetration welding [6]; Volpp J. studied the formation mechanism of hole splash in laser deep penetration welding [7]; Katayama S. et al. researched high-power fiber laser welding [8] and welding defect prevention procedures [9]; Moskvitin G. V. performed some surveys on the industrial application of laser welding [10]; Robertson S. M. et al. investigated the material loss caused by keyholes in laser welding [11]. In their research, they all found that too high laser power will cause many problems in the welding process, such as spatter, porosity, and unstable keyholes, which will lead to a decline in the welding quality. Reducing the ambient pressure to increase the weld penetration depth and improve the quality of the joint is a good option.

Since 2001, the laser welding process under sub-atmospheric pressures has attracted much attention, and many studies have focused on it. Katayama et al. [12,13] found that laser welding under sub-atmospheric pressures can increase the penetration depth and prevent welding porosity for stainless steel and aluminum alloys. Christian Börner et al. [14] found that reducing the ambient pressure can reduce spattering, and the welding seams could be achieved qualitatively equal to those of an electron beam weld seam. M. Jiang et al. [15] found that laser welding under vacuum showed excellent weld quality and a wide processing window. Chen X. et al. [16] reported that reducing the ambient pressure during welding helps to obtain Ti/Al dissimilar joints with excellent tensile properties and a uniform IMCs distribution. Many studies showed that reducing the ambient pressure can effectively increase the penetration depth and weld quality [17].

For the Ti-6Al-4V alloy, the light element aluminum has a low boiling point and is easy to evaporate. In recent years, it has been reported that high-energy beam processing under vacuum causes the evaporation of elements with low boiling points from the alloy and their uneven distribution in the fusion zone. This problem was first found during the electron beam melting of titanium alloys. V. G. Ivanchenko and Akhonin et al. [18,19] have separately found that aluminum evaporates rapidly during the electron beam melting of Ti-Al alloys and have developed a mathematical model to describe it. Wang et al. [20] reported that an uneven distribution of elements due to the evaporation of magnesium occurred in the welds of 5A06 aluminum alloy obtained by laser welding under vacuum. V. Juechter and A. Klassen et al. [21–23] separately focused on the evaporation of aluminum during the selective electron beam melting (SEBM) of Ti-Al alloys and provided a method to calculate elemental evaporation fluxes.

At present, there are few studies about the evaporation of light elements in the high-power vacuum laser welding process. It is unclear how aluminum evaporates from the keyhole wall under vacuum and is distributed in the weld seam. The loss and uneven distribution of aluminum in the fusion zone will affect the joint's microstructure and mechanical properties [24,25]. For vacuum laser welding where the penetration depth is large, this influence will be more significant. Therefore, it is necessary to study the evaporation and distribution of aluminum during the vacuum laser welding of Ti-6Al-4V alloys.

Furthermore, most of the simulation studies of elemental evaporation used two-dimensional models. For keyhole welding, due to the complex and frequent oscillations of the liquid surface, it is difficult for a two-dimensional model to indicate the shape of the liquid surface. In addition, due to the high temperature of the wall surface in front of the keyhole, the evaporation is intense, but it is hard to describe this using a two-dimensional model. It is necessary to build a 3D model to observe the morphology of the keyhole and the temperature and evaporation flux fields from different angles.

This paper focuses on the uneven distribution of aluminum due to evaporation during laser vacuum welding of Ti-6Al-4V alloys. The study was carried out using a combination of experiments and simulations. Vacuum laser welding was carried out on Ti-6Al-4V alloy plates. The composition of the vapor generated by the welding process and the distribution of aluminum in the weld cross-section were examined. A three-dimensional model of the laser keyhole welding process in a vacuum environment was built. The keyhole shape, temperature field, and the evaporation flux field of vacuum laser welding under different process parameters were obtained.

2. Materials and Methods

To explore the influence of process parameters on the alloy elements' evaporation and distribution in the weld seam, vacuum laser welding on Ti-6Al-4V plate was conducted with the setup shown in Figure 1. The workpieces were placed in a vacuum chamber during the welding process. The window of the top cover is covered with quartz glass to allow the laser beam to pass through. A vacuum pump and a pressure gauge were connected to the chamber to maintain a stable ambient pressure. A 30 kW IPG YLS-30000-SS4 fiber laser with a wavelength of 1070 nm and spot diameter of 0.3 mm was used as the welding source. The incident angle of the laser beam was set to 10°, and the defocus distance was 0 mm.

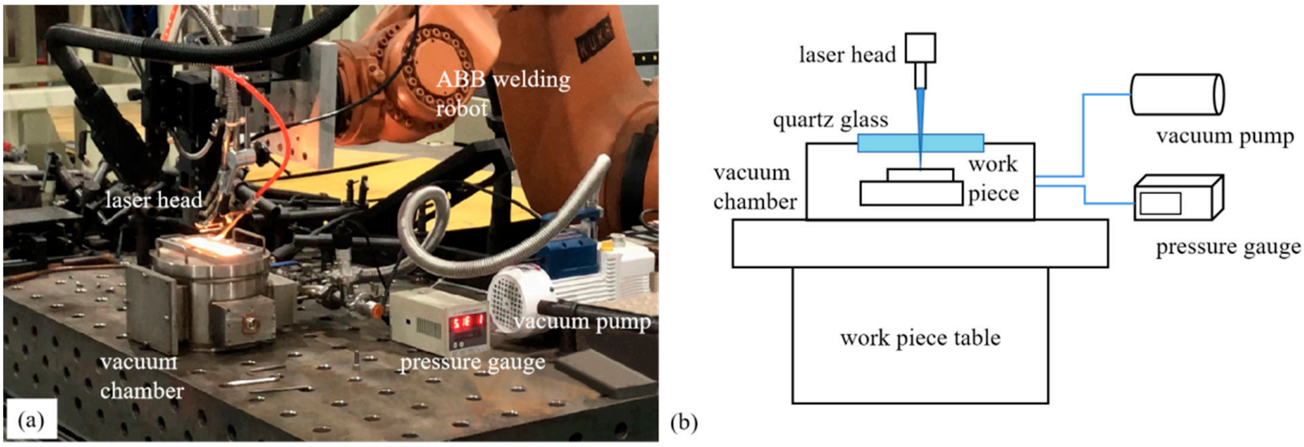

Figure 1. Vacuum laser welding system. (**a**) Actual experimental apparatus; (**b**) Simplified diagram of welding system.

Laser vacuum welding was performed on Ti-6Al-4V plates of size 150 mm × 80 mm × 20 mm. The composition of the alloy is shown in Table 1. Considering the systematic nature of the research and the stability of the instrument, welding tests with different laser power and welding speed were carried out. The specific process parameters are shown in Table 2.

Table 1. The chemical composition of the Ti-6Al-4V alloy (wt.%).

Al	C	H	N	O	V	Ti
5.5–6.5	0.08	0.015	0.030	0.20	3.5–4.5	Bal.

Table 2. Process parameters of vacuum laser welding.

Process Number	Laser Power (kW)	Welding Speed (m/min)
1	6	2
2	8	2
3	10	1
4	10	1.5
5	10	2
6	10	2.5
7	10	3
8	12	2
9	14	2
10	16	2
11	18	2

To investigate the alloy elements' evaporation during laser vacuum welding, the chemical composition of the metal vapor and weld seam under different process parameters were detected by X-ray fluorescence (XRF) and Electron Probe Microanalysis (EPMA) equipment, respectively. During the welding process, metal vapor left the workpieces and condensed on the quartz glass plate placed above the weld. The chemical composition of the metal vapor was detected by examining the composition of the metal deposited on the glass plate. The glass plate was examined using XRF. To investigate the chemical composition of the weld at different depths, weld cross-section samples were prepared and tested by EPMA. Specimens with the dimensions 15 mm × 8 mm × 20 mm were cut perpendicular to the weld beam, and the weld cross-sections were polished with sandpaper.

Five locations of each sample were taken at equal distances, between 1 mm from the upper surface of the workpieces and 5 mm from the bottom of the fusion zone. An EPMA line scan was performed on the weld cross-section parallel to the direction of the flat surface. The examining method and data point selection are shown in Figure 2.

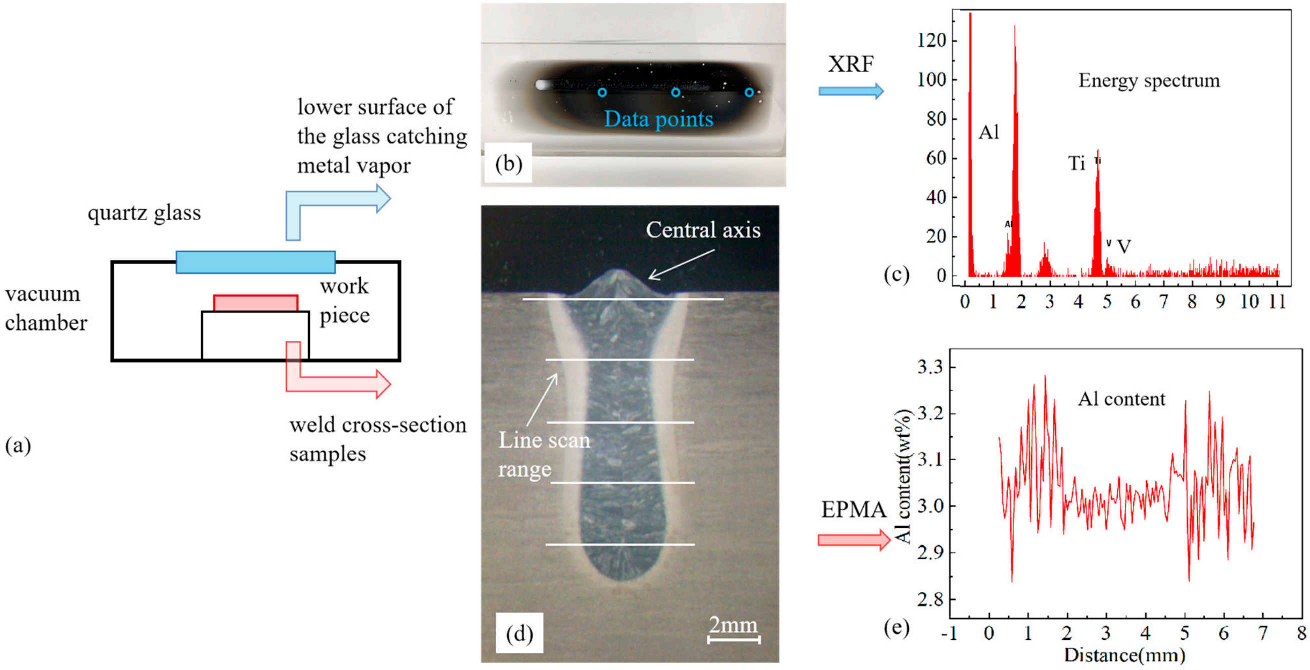

Figure 2. Figure 2. Examining method and data point selection. (**a**) Welding system; (**b**) quartz glass after welding, covered with metal vapor; (**c**) XRF result of metal vapor; (**d**) weld cross-section sample and line scan position; (**e**) EPMA line scan result of the weld seam.

3. Numerical Simulations

The evaporation flux during the vacuum laser welding process was calculated using the numerical simulation method to explain the experimental results. The keyhole surface morphology was calculated based on the level set method [26–28], and the evaporation flux fields of Ti and Al on the keyhole surface were calculated using a multi-component evaporation model [10,11].

3.1. Thermodynamic and Hydrodynamic Model

To accurately characterize the keyhole morphology and the evaporation behavior of the Al during vacuum laser welding, reliable heat transfer and fluid flow models must be established. In this model, it is assumed that molten metal liquid is incompressible; heat transfer and fluid flow in the melt pool is calculated by solving the following equations:

$$\begin{gathered}
\nabla\cdot\vec{U} = 0 \\
\rho\left(\frac{\partial\vec{U}}{\partial t} + (\vec{U}\cdot\nabla)\vec{U}\right) = \nabla\cdot(\mu_1\nabla\vec{U}) - \nabla p - \frac{\mu_1}{K}\vec{U} - \frac{C\rho}{\sqrt{K}}|\vec{U}|\vec{U} + \rho\vec{g}\beta(T - T_{ref}) \\
\rho C_p\left(\frac{\partial T}{\partial t} + (\vec{U}\cdot\nabla)T\right) = \nabla\cdot(K\nabla T),
\end{gathered} \tag{1}$$

where $\vec{U}$ represents the velocity, ρ, p, μ_1, $\vec{g}$, β, C_p, and k represent the density, pressure, viscosity, gravitational vector, thermal expansion coefficient, heat capacity, and heat conductivity, and T and T_{ref} represent the temperature and reference temperature. C is an inertial parameter related to the liquid fraction f_l, $C = 0.13f_l^{-3/2}$. K is the Carman–Kozeny coefficient of the mixture model.

On the keyhole wall, the heat transfer equation includes Fresnel absorption, heat conduction, and evaporation terms. The energy boundary conditions can be described as:

$$k\frac{\partial T}{\partial \vec{n}} = q - h(T - T_\infty) - \varepsilon_r \sigma_s \left(T^4 - T_\infty^4\right) - \rho V_{evp} L_v, \tag{2}$$

where q is the energy absorbed by Fresnel absorption, h, ε_r, σ_s, V_{evp} and L_v are the heat convection coefficient, black body radiation coefficient, Stefan–Boltzmann coefficient, keyhole interface recession speed due to evaporation, and evaporation latent heat. On other surfaces, without laser irradiation, the energy boundary conditions can be described as:

$$k\frac{\partial T}{\partial \vec{n}} = -h(T - T_\infty) - \varepsilon_r \sigma_s \left(T^4 - T_\infty^4\right). \tag{3}$$

Using the level set method to track the keyhole free surface evolutions, the time-dependent keyhole profiles can be described as:

$$\frac{\partial \phi}{\partial t} + \vec{U} \cdot (\nabla \phi) = 0. \tag{4}$$

3.2. Multi-Component Evaporation Model

The evaporation flux on the molten pool surface is mainly related to the surface temperature and saturation pressure for certain alloys. Considering the role of the Knudsen layer at the gas–liquid interface, in a multi-component system, the partial fluxes of an alloying element are given by [22,23]:

$$j_{net}^{\alpha} = \varnothing \cdot \chi^{\alpha} \cdot \gamma_{act}^{\alpha}(T_s, \chi^{\alpha}) \cdot p_s^{\alpha}(T_s) \cdot \sqrt{\frac{m_A^{\alpha}}{2\pi \cdot k_B T_s}}, \tag{5}$$

in which $\varnothing$ denotes the evaporation coefficient. For a high laser intensity under low ambient pressure with high evaporation rates, $\varnothing = 0.82$. χ^{α}, γ_{act}^{α}, p_s^{α} and m_A^{α} represent the composition, activity coefficient, saturated vapor pressure, and atomic mass of the alloy element α. T_s is the surface temperature, and k_B is Boltzmann's constant.

As the boiling temperature of vanadium is much higher than the other alloy elements, in this work, consider the binary alloy system Al-Ti. The activity coefficients of an element can be calculated by [22,23]:

$$\gamma_{act}^{\alpha}(T_s, \chi) = \exp\left(\frac{\Delta G_{\Gamma}^{\alpha}(T_s, \chi)}{R_g T_s}\right), \tag{6}$$

where R_g represents the gas constant. $\Delta G_{\Gamma}^{\alpha}(T_s, \chi)$ represents the partial excess Gibbs free energy of element α in the binary mixture, which can be calculated as follows [22,23]:

$$\Delta G_{Al,\,Ti}^{Al} = \Delta G_{Al,Ti}(T_s, \chi) + \left(1 - \chi^{Al}\right) \cdot \frac{\partial \Delta G_{Al,Ti}(T_s, \chi)}{\partial \chi^{Al}}, \tag{7}$$

$$\Delta G_{Al,\,Ti}^{Ti} = \Delta G_{Al,Ti}(T_s, \chi) - \chi^{Al} \cdot \frac{\partial \Delta G_{Al,Ti}(T_s, \chi)}{\partial \chi^{Al}}. \tag{8}$$

The keyhole surface temperature, T_s, is obtained by solving the heat transfer and fluid flow equations for the molten pool. $p_s^{\alpha}(T_s)$ means the saturated vapor pressure at the liquid surface of alloy element α. Due to the large length of the keyholes in vacuum laser welding, the keyhole surface's pressure balance and evaporation schematics are different from processes with shallower melt depths, such as laser ablation. For the characteristics of laser keyhole welding, a specialized method was chosen to calculate the saturation pressure on the liquid surface. Many studies have proposed a variety of ways for solving the saturated vapor pressure at the keyhole surface in laser welding [26,29–32]. Combined with the experimental results, the following expression was selected:

$$P_{sat}(T_s) = P_0 \exp\left(L_v \frac{T_s - T_b}{R_g T_s T_b}\right), \tag{9}$$

in which P_0 represents the atmospheric pressure,T_b represents the boiling temperature, T_s is the surface temperature, L_v represents the latent heat of evaporation, and R_g represents the ideal gas constant.

Evaporation only happens at the surface of the molten liquid, where the vapor pressure of element α exceeds the external pressure. Using partial net evaporation fluxes, the evaporation amount of a single component α during Δt at a single cell of size Δx can be calculated as follows:

$$\Delta m^{\alpha}_{vap}(X_s,\ t) = j^{\alpha}_{net}(X_s,\ t)\Delta x^2 \Delta t. \tag{10}$$

Thus, the mass loss due to evaporation of a single element α for each surface cell during that time step, $\Delta m^{\alpha}_{vap}(X_s,\ t)$, can be calculated.

3.3. Numerical Implementation

Numerical simulations were carried out in three dimensions. The computational domains were 6 mm × 10 mm × 30 mm, and the plate thickness was 20 mm. The grid size was x = 0.1 mm and the time step was determined by the Courant–Friedrichs–Lewy (CFL) condition and did not exceed 10^{-5} s.

In the calculation of multi-component evaporation, only two elements, Ti and Al, were considered. The system is regarded as a binary alloy. For the Ti-6Al-4V alloy, the parameters used in the calculation are shown in Table 3 [22,23].

Table 3. Physical properties of Ti–6Al–4V used in the numerical simulations.

Property	Value
Density, liquid ($kg \cdot m^{-3}$)	4122
Dynamic viscosity ($m \cdot Pas$)	4.76
Surface tension ($J \cdot m^{-2}$)	1.52
T_{sol} (K)	1878
T_{liq} (K)	1928
T^{Ti}_{boil} (K)	3558
T^{Al}_{boil} (K)	2726
T^{Ti}_{crit} (K)	7890
T^{Al}_{crit} (K)	6700
$C_{p,s}$,mean ($J \cdot kg^{-1} \cdot K^{-1}$)	670
$C_{p,l}$ ($J \cdot kg^{-1} \cdot K^{-1}$)	1126
L_{fus} ($kJ\ kg^{-1}$)	290
$L^{Ti}_{vap,0}$ ($MJ\ kg^{-1}$)	9.7
$L^{Al}_{vap,0}$ ($MJ\ kg^{-1}$)	11.6

Numerical simulations were carried out for a laser power of 10 kW, welding speed of 1, 2, 3 m/min, and welding speed of 2 m/min with laser powers of 6, 12, and 18 kW, respectively.

4. Result

From the previous theory, it can be seen that the evaporation flux is influenced by the surface temperature and the saturation air pressure, which are closely related to the welding process parameters. To investigate the uneven distribution of aluminum caused by the evaporation of the light elements during vacuum laser welding, the chemical composition of the metal vapor and the distribution of aluminum in the fusion zones of the welded workpieces under different process parameters were focused on.

4.1. Composition of Metal Vapor

The chemical composition of the metal vapor leaving the keyhole due to evaporation was detected from the metal deposits on the quartz glass plate placed above the workpiece during welding processing. For each sample, three points were selected with a diameter of 50 μm and their results were averaged to give the results for that sample. The experimental results are shown in blue in Figure 3.

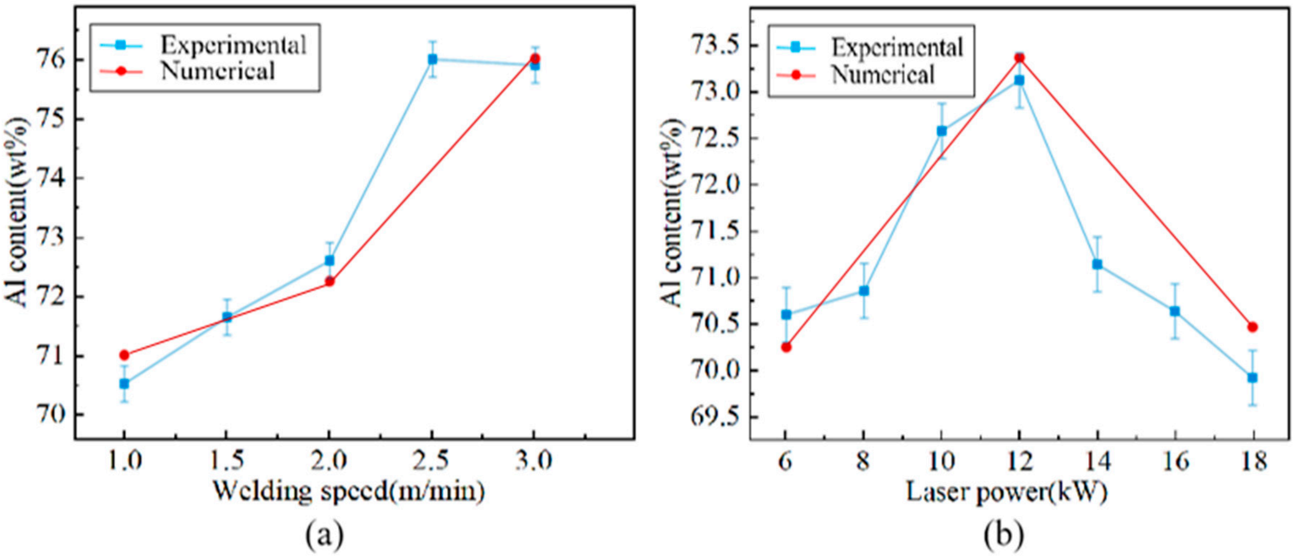

Figure 3. The chemical composition measured by experiments (blue) and calculated by the numerical simulation method (red) of the metal vapor with (**a**) different welding speeds and (**b**) different laser powers.

When the laser power was fixed, the aluminum content in the metal vapor increased with the welding speed. When the welding speed was fixed, the aluminum content in the metal vapor increased with the laser power when it was below 12 kW and then decreased when it exceeded 12 kW. This is caused by the inconsistent increase in the evaporation rates of titanium and aluminum when the surface temperature of the keyhole rises with the heat input. When the laser power is increased, the aluminum content in the metal vapor increases first and then decreases, which is caused by the inconsistent increase in the evaporation rates of titanium and aluminum when the surface temperature of the keyhole rises with the heat input. Titanium has a higher melting point and aluminum has a lower melting point. When the laser power rises from 6 kW to 12 kW, the increase in power makes the evaporation of aluminum become very intense, while the increase in the evaporation rate of titanium is relatively small. When the laser power is increased from 12 kW to 18 kW, the evaporation of titanium is intensified under the higher heat input, and the increase in the aluminum evaporation flux is relatively small.

To verify the model's accuracy, the ratio of the total amount of Ti and Al evaporated under different process parameters was calculated and compared with the experimental results. The evaporation flux on each cell of the keyhole surface can be calculated using Equations (5)–(10). Further, the total evaporated mass of a single element α can be obtained by summing the evaporated amount of all cells on the surface of the keyhole:

$$\Delta m^{\alpha}_{vap,total} = \sum \Delta m^{\alpha}_{vap}(X_s,\ t). \tag{11}$$

The mass fraction of aluminum in the metal vapor is obtained by comparing the total evaporation of the two elements. The results calculated by the above equation under different process parameters are shown in red in Figure 3. It is found that the simulation results match the experimental results.

4.2. Uneven Distribution of Elements in the Welding Seam

To show the distribution of aluminum in the weld, the mean value of the data obtained from the EPMA line scan was used to represent the average aluminum concentration at that depth. Data points within 2 mm to 7 mm from the center of the weld were taken as the average value of the aluminum content at that depth to avoid macroscopic segregation in the weld affecting the results. The data acquisition method is shown in Figure 4. The results of other samples can be obtained in the same way.

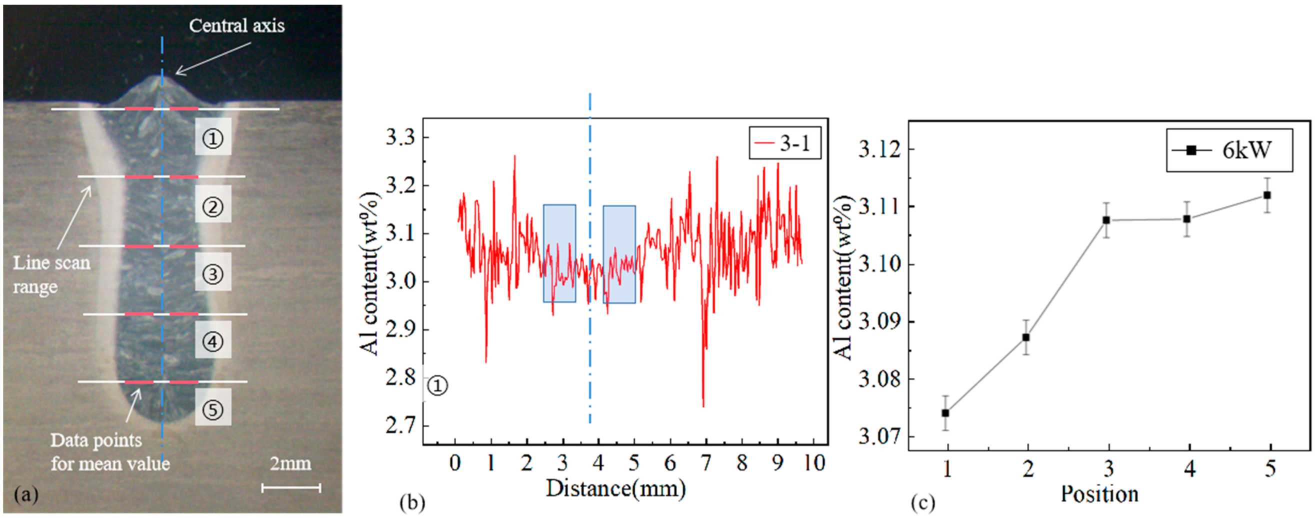

Figure 4. (**a**) Data selection range on weld sections; (**b**) data selection range for EPMA line scan results (take ① for example); (**c**) detection results of aluminum concentration with depth.

The distribution of aluminum in the fusion zone at different welding speeds and different laser powers are shown in Figures 5 and 6. It can be seen that when the welding speed was low, the Al content at the deeper position of the fusion zone was higher than that closer to the keyhole exit. When the welding speed increased, the peak Al content gradually moved upward and appeared in the middle of the weld. As the welding speed increased, the distribution of the aluminum became more uneven. For samples of different laser powers, the Al concentration showed an increasing trend from the surface to the bottom of the welds and showed a peak at the middle of the welds. The most uneven distribution of Al was observed at a laser power of 12 kW. At this power, the concentration of Al in the metal vapor was the highest.

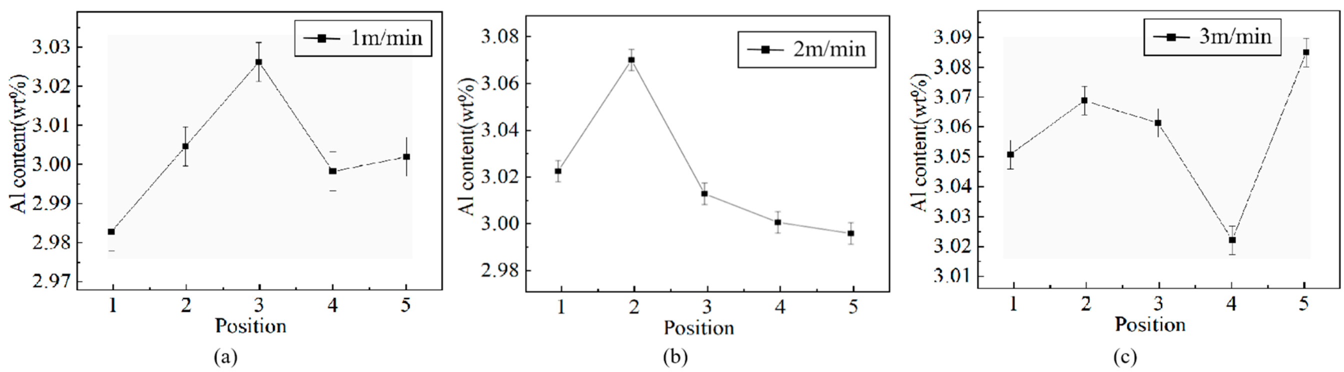

Figure 5. Distribution trend of Al for different welding speeds: (**a**) 1 m/min; (**b**) 2 m/min; (**c**) 3 m/min.

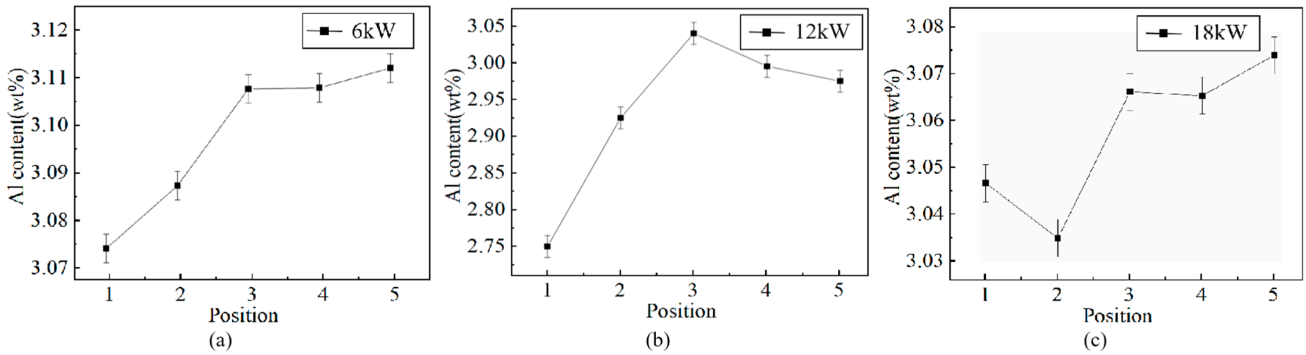

Figure 6. Distribution trend of Al for different laser powers: (**a**) 6 kW; (**b**) 12 kW; (**c**) 18 kW.

To measure the uneven distribution of aluminum in the weld, a variable K was introduced:

$$K = \frac{\omega_{max}^{Al} - \omega_{min}^{Al}}{\omega_{avg}^{Al}}, \quad (12)$$

where ω_{max}^{Al}, ω_{min}^{Al}, and ω_{avg}^{Al} indicate the maximum, minimum, and average values of the aluminum content in the weld, respectively. The larger the value of K, the more uneven the distribution of aluminum in the weld. The calculated results of the K values for different welding speeds and laser powers, compared with the Al content in the metal vapor, are shown in Figure 7.

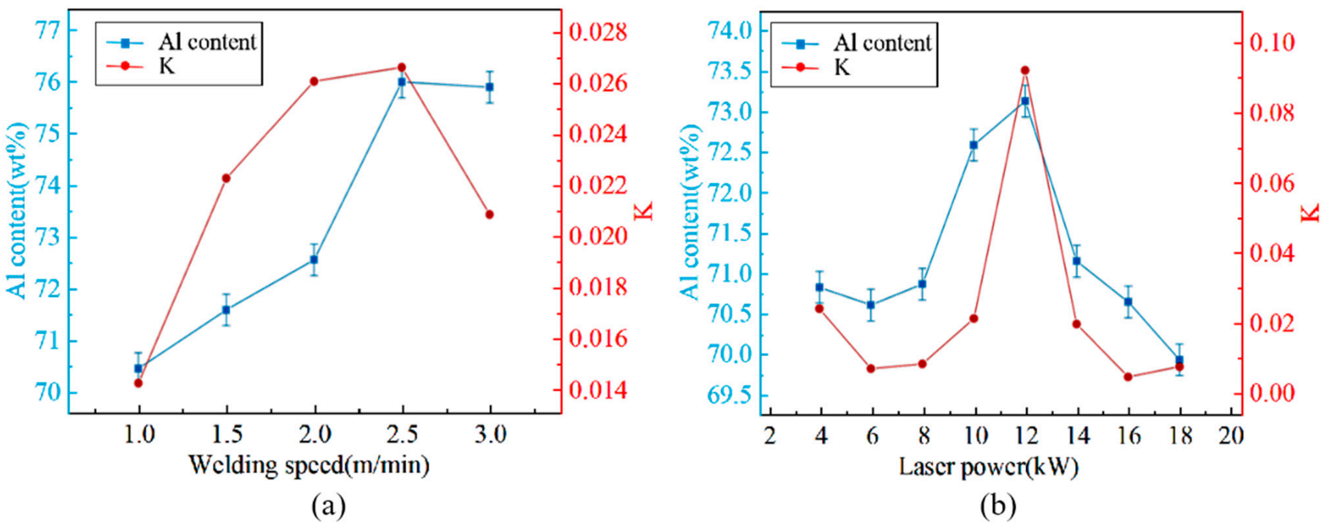

Figure 7. Calculated results of the K values at different welding speeds (**a**) and different laser (**b**) powers.

When the welding speed rose from 1 m/min to 2.5 m/min, the value of K rose from 0.0146 to 0.0274 and then fell to 0.214 when the welding speed rose to 3/min. When the laser power rose from 6 kW to 12 kW, the value of K rose from 0.012 to 0.10 and then fell to 0.0128 when the laser power rose to 18 kW.

It can be seen that the trend of K was consistent with the aluminum content in the metal vapor, which suggests that the main cause of the uneven distribution of aluminum in the weld is the behavior of the vapor and keyhole morphology. During welding, part of the metal vapor generated from the keyhole wall cannot leave the workpiece and, thus, remains in the fusion zone. This could be the main reason for the uneven distribution of aluminum in it.

5. Discussion

To explain the experimental results, consider the actual process of vacuum laser welding. The keyhole shape and metal evaporation during the vacuum laser welding process are difficult to observe directly. Thus, numerical simulation methods were used to analyze the evaporation location and evaporation amount of Al and Ti. Then, whether the metal vapor can leave the workpiece was analyzed by observing the morphology of the keyhole.

5.1. Effect of Process Parameters on the Evaporation Field at the Keyhole Wall

From previous theoretical analysis, it is known that the evaporation of elements during the welding process is mainly related to the keyhole surface temperature. The relationship between the evaporation fluxes at a single cell of the two elements Ti and Al and the temperature can be calculated using Equations (6)–(10). The results are shown in Figure 8. It can be seen that when the keyhole surface temperature rises, the evaporation flux of both elements rises rapidly. When the temperature exceeds 2500 K, Al evaporates significantly, while only when the temperature exceeds 3000 K does Ti start to evaporate significantly.

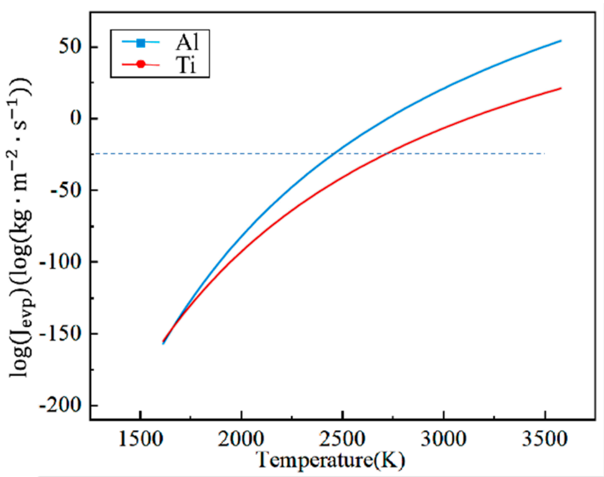

Figure 8. Variation in Ti and Al evaporation flux in the alloy with temperature.

Figure 9 shows the simulation results of the keyhole shape and its surface temperature and the evaporation fields of Al and Ti under different welding speeds. When the welding speed increases from 2 m/min to 3 m/min, the molten pool length and keyhole diameter increase, the area for evaporation increases, and it is easier for metal vapor to leave the workpiece, therefore, the evaporation of Al is greater. When the welding speed reduces to 1 m/min, the temperature of the keyhole wall decreases, which leads to a decrease in the evaporation of Al, this may be due to the longer length of the keyhole dispersing the laser energy.

Figure 10 shows the simulation results of the keyhole shape and its surface temperature field and the evaporation field of Al and Ti under different laser powers. While the laser power is less than 12 kW, the evaporation of Al increases as the laser power increases, while the evaporation of Ti is negligible. When the laser power exceeds 12 kW and continues to rise, the keyhole surface is seriously overheated. The evaporation of Ti increases sharply, resulting in a decrease in the proportion of Al in the metal vapor.

5.2. Effect of Process Parameters on the Distribution of Aluminum in the Weld Seam

The highest temperature and most intense evaporation usually occur at the bottom of the keyhole and the wrinkles of the keyhole front wall. The laser energy concentration is caused by the low ambient pressure [33–35]. It has been shown that when the ambient pressure drops below 103 Pa, the scattering effect of the plasma plume on the laser almost disappears, so the laser energy can be delivered directly to the bottom of the keyhole.

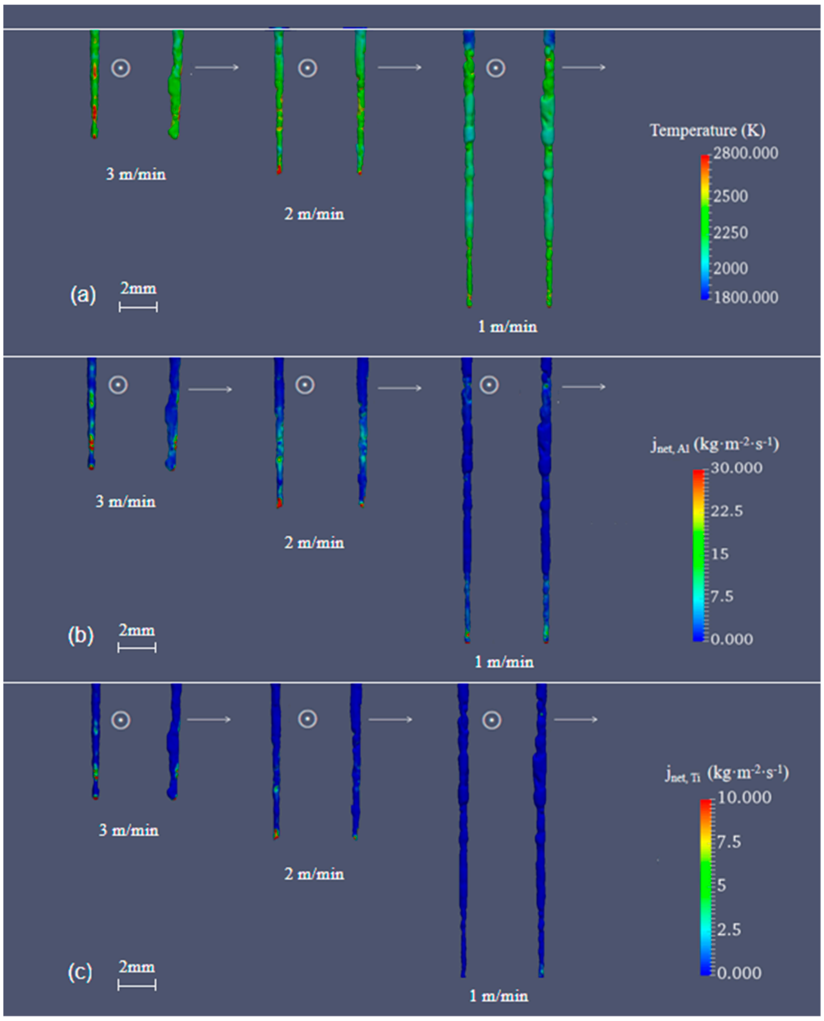

Figure 9. Simulation results: The keyhole shape and its (**a**) surface temperature field, and the evaporation fields of (**b**) Al and (**c**) Ti under different welding speeds. Where ⊙ and → refer to the welding direction.

If the keyhole remains open, parts of the metal vapor generated from the keyhole wall leave through the exit, and parts of it are absorbed by the molten pool as the rear wall of the keyhole moves forward. The shallow position of the fusion zone is closer to the keyhole exit, and the metal vapor is more likely to escape. While deep in the keyhole, it is difficult for the metal vapor to leave, although the evaporation is more intense. So, the Al content of the fusion zone usually increases with increasing depth. The fracture or necking of the keyhole could lead to the peak in Al content observed in the middle of the fusion zone. It will block the metal vapor generated below it, thus enriching the Al at that location. At the same time, the fracture will also cause a new temperature and evaporation peak above it, thus increasing the amount of Al evaporation there.

The effect of the moving speed of the keyhole on the aluminum distribution when the welding speed is varied is considered. Figure 11 shows the keyhole shape at different welding speeds. When the welding speed rises, the keyhole length reduces, and its diameter and inclination increase. For welding speeds from 2 to 3 m/min, as shown in Figure 11a,b, the keyhole rear wall shows a backward protrusion caused by the metal vapor impacting the rear wall surface. The molten pool absorbs the metal vapor, resulting in a peak in aluminum content at this position. When the welding speed is 1 m/min, as shown in Figure 11c, the keyhole is vertical, but the keyhole length is larger, and the diameter is smaller. It becomes difficult for the metal vapor to leave the keyhole. Thus, the aluminum becomes enriched in the bottom of the fusion zone.

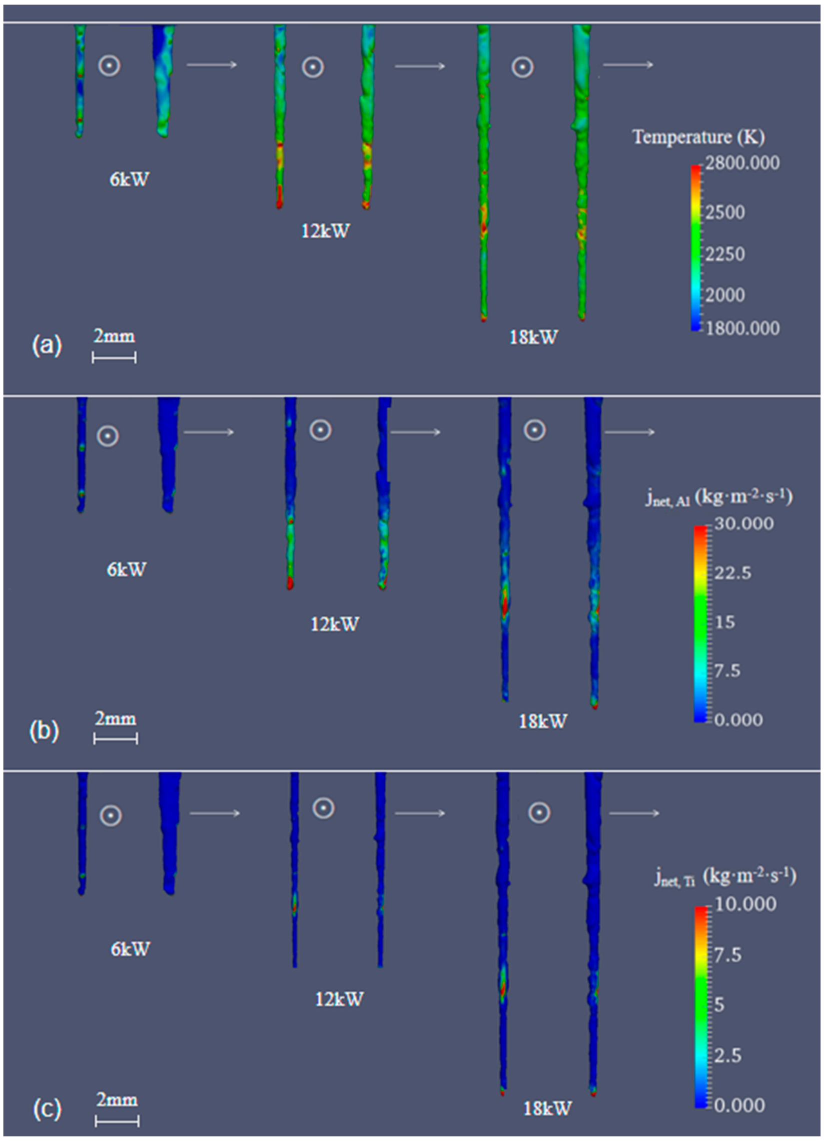

Figure 10. Simulation results: The keyhole shape and its (**a**) surface temperature field, and the evaporation fields of (**b**) Al and (**c**) Ti under different laser powers. In which ⊙ and → refer to the welding direction.

When the laser power is changed, the effect of the keyhole stability on the aluminum distribution is considered. Figure 12 shows the keyhole shape at different laser powers. When laser welding is performed at low power, the keyhole is more stable, so the metal vapor can leave smoothly. Thus, the concentration of Al in the fusion zone increases in the depth direction, as shown in Figure 12a. When the laser power is 12 kW, the keyhole begins to narrow and wrinkles appear in the middle part of the keyhole, as shown in Figure 12b, so the distribution of aluminum shows a trend of rising and then falling. When the laser power rises to 18 kW, the Al distribution fluctuates more randomly with the change of melting depth because of the violent oscillation of the keyhole and the frequent occurrence of necking and fracture, as shown in Figure 12c. This will cause noticeable evaporation in the middle part of the keyhole and frequent position changes.

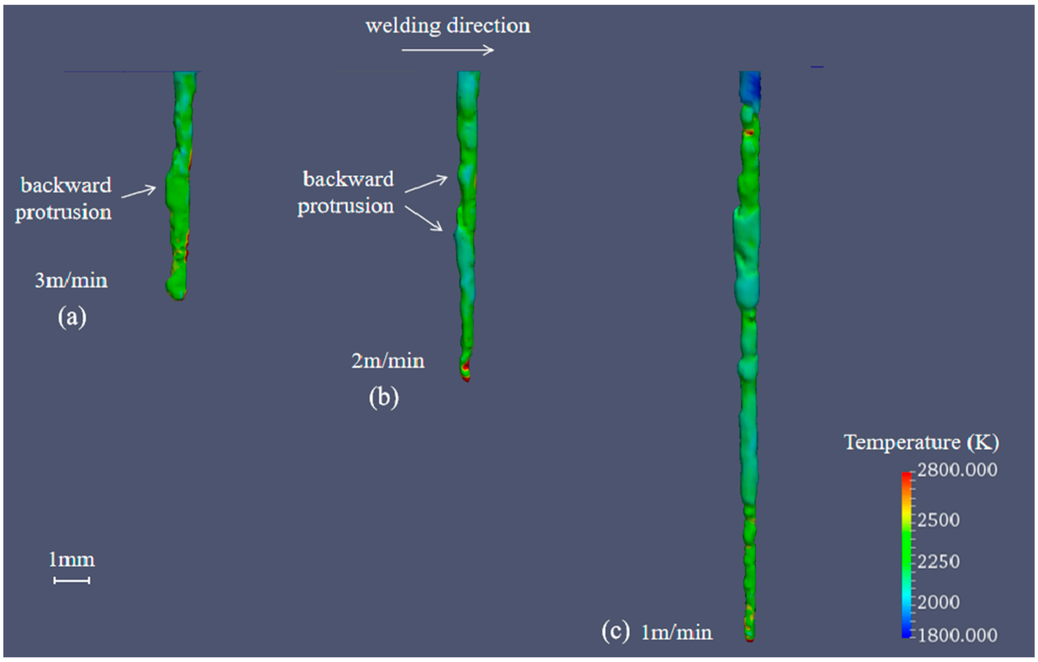

Figure 11. Different keyhole shapes at different welding speeds: (**a**) 1 m/min; (**b**) 2 m/min; (**c**) 3 m/min.

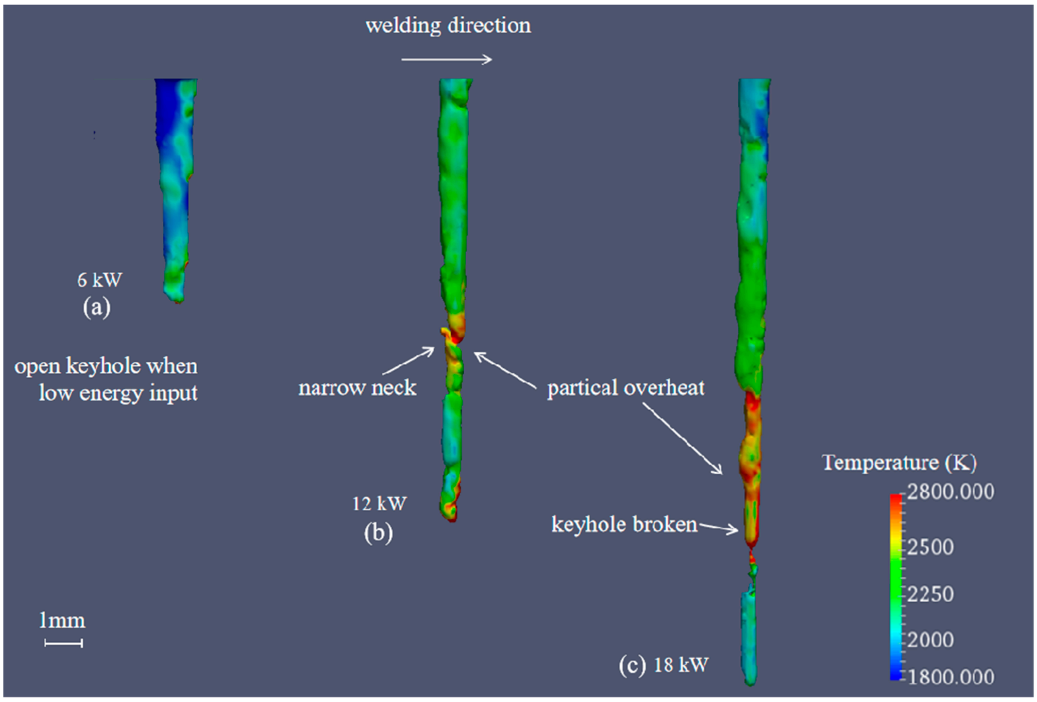

Figure 12. Different keyhole shapes at different laser powers: (**a**) 6 kW; (**b**) 12 kW; (**c**) 18 kW.

6. Conclusions

For the vacuum laser welding process of the Ti-6Al-4V alloy, a combination of experiments and simulations was used to study the influence of process parameters on evaporation and the uneven distribution of Al. The composition of the metal vapor leaving the workpiece at different welding speeds and laser powers was detected. The distribution of aluminum at different depths of the fusion zone at different welding speeds and laser powers was examined. The temperature and evaporation flux fields of the keyhole surface and the ratios of the total evaporation fluxes of Ti and Al were obtained by numerical simulation. The following conclusions were drawn:

- When the welding speed is fixed, the relative loss of aluminum increases gradually with the laser power from 6 to 18 kW. It gradually increases and reaches a peak at 12 kW, the aluminum mass fraction of the metal vapor reaches 73.0%, and then gradually decreases. When the laser power is constant, the relative loss of aluminum increases gradually with the welding speed from 1 to 3 m/min, and reaches a peak at 2.5 m/min. The mass fraction of aluminum in the metal vapor is about 75.7%, and then remains stable.
- The trend of the unevenness of the Al distribution in the weld with the process parameters was in basic agreement with the trend of the Al content in the metal vapor. The uneven distribution of aluminum in the weld is related to the keyhole morphology and the behavior of the metal vapor in the keyhole.
- In general, the content of aluminum at the bottom of the fusion zone is higher than at the top. However, the peak of aluminum content may also appear in the middle of the weld if the metal vapor cannot leave the keyhole smoothly. When the keyhole rear wall shows a backward protrusion or the keyhole becomes narrow, aluminum is enriched at that position.

Author Contributions: Conceptualization, X.T., Z.L. and A.H.; Methodology, B.W. and L.L.; Software, S.Z. and L.L.; Validation, B.W. and Y.L.; Resources, A.H.; Data curation, S.Z. and X.T.; Writing—original draft, S.Z.; Writing—review & editing, B.W., X.T., Y.L. and L.L.; Supervision, Z.L. and A.H.; Project administration, Z.L.; Funding acquisition, A.H. All authors have read and agreed to the published version of the manuscript.

Funding: This research is financially supported by the National Science Fund for Excellent Young Scholars (NSFC) (No. 52022033), and the National Natural Science Foundation of China (NSFC) (No. 52005193).

Data Availability Statement: Not applicable.

Conflicts of Interest: The authors declare no conflict of interest.

References

1. Peters, M.; Kumpfert, J.; Ward, C.H.; Leyens, C. Titanium alloys for aerospace applications. *Adv. Eng. Mater.* **2003**, *5*, 419–427. [CrossRef]
2. Patnaik, A.; Poondla, N.; Bathini, U.; Srivatsan, T.S. On the use of gas metal arc welding for manufacturing beams of commercially pure titanium and a titanium alloy. *Mater. Manuf. Process.* **2011**, *26*, 311–318. [CrossRef]
3. Oryshchenko, A.S.; Gorynin, I.V.; Leonov, V.P.; Kudryavtsev, A.S.; Mikhailov, V.I.; Chudakov, E.V. Marine titanium alloys: Present and future. *Inorg. Mater. Appl. Res.* **2015**, *6*, 571–579. [CrossRef]
4. Kumar, V.A.; Gupta, R.K.; Prasad, M.; Murty, S.V.S.N. Recent advances in processing of titanium alloys and titanium aluminides for space applications: A review. *J. Mater. Res.* **2021**, *36*, 689–716. [CrossRef]
5. Dhinakaran, V.; Shriragav, S.V.; Fahmidha, A.F.Y.; Ravichandran, M. A review on the categorization of the welding process of pure titanium and its characterization. *Mater. Today Proc.* **2020**, *27*, 742–747. [CrossRef]
6. Zhu, B.; Zhang, G.; Zou, J.; Ha, N.; Wu, Q.; Xiao, R. Melt flow regularity and hump formation process during laser deep penetration welding. *Opt. Laser Technol.* **2021**, *139*, 106950. [CrossRef]
7. Volpp, J. Formation mechanisms of pores and spatters during laser deep penetration welding. *J. Laser Appl.* **2017**, *30*, 12002. [CrossRef]
8. Katayama, S.; Kawahito, Y. Elucidation of phenomena in high-power fiber laser welding and development of prevention procedures of welding defects. In *Fiber Lasers VI: Technology, Systems, and Applications*; International Society for Optics and Photonics: Bellingham, WA, USA, 2009; Volume 7195, p. 71951R. [CrossRef]
9. Katayama, S.; Kawahito, Y.; Mizutani, M. Elucidation of laser welding phenomena and factors affecting weld penetration and welding defects. *Phys. Procedia* **2010**, *5*, 9–17. [CrossRef]
10. Moskvitin, G.V.; Polyakov, A.N.; Birger, E.M. Application of laser welding methods in industrial production. *Weld. Int.* **2013**, *27*, 572–580. [CrossRef]
11. Robertson, S.M.; Kaplan, A.F.H.; Frostevarg, J. Material ejection attempts during laser keyhole welding. *J. Manuf. Process.* **2021**, *67*, 91–100. [CrossRef]
12. Katayama, S.; Kobayashi, Y.; Mizutani, M.; Matsunawa, A. Effect of vacuum on penetration and defects in laser welding. *J. Laser Appl.* **2001**, *13*, 187–192. [CrossRef]

13. Katayama, S.; Yohei, A.; Mizutani, M.; Kawahito, Y. Development of deep penetration welding technology with high brightness laser under vacuum. *Phys. Procedia* **2011**, *12*, 75–80. [CrossRef]
14. Börner, C.; Dilger, K.; Rominger, V.; Harrer, T.; Krüssel, T.; Löwer, T. Influence of ambient pressure on spattering and weld seam quality in laser beam welding with the solid-state laser. In *International Congress on Applications of Lasers & Electro-Optics*; Laser Institute of America: Orlando, FL, USA, 2011; pp. 621–629. [CrossRef]
15. Jiang, M.; Tao, W.; Chen, Y.; Li, F. Comparison of processing window in full penetration laser welding of thick high-strength steel under atmosphere and sub-atmosphere. *Opt. Laser Technol.* **2019**, *109*, 449–455. [CrossRef]
16. Chen, X.; Lei, Z.; Chen, Y.; Han, Y.; Jiang, M.; Tian, Z.; Bi, J.; Lin, S. Microstructure and tensile properties of Ti/Al dissimilar joint by laser welding-brazing at subatmospheric pressure. *J. Manuf. Process.* **2020**, *56*, 19–27. [CrossRef]
17. Yang, F.; Xia, G.; Guo, X.; Chen, C.; Long, Y.; Chen, B.; Tang, J.; Chen, G. Research progress of laser welding under subatmospheric pressure. *Int. J. Adv. Manuf. Technol.* **2021**, *116*, 803–820. [CrossRef]
18. Ivanchenko, V.G.; Ivasishin, O.M.; Semiatin, S.L. Evaluation of evaporation losses during electron-beam melting of Ti-Al-V alloys. *Metall. Mater. Trans. B* **2003**, *34*, 911–915. [CrossRef]
19. Akhonin, S.V.; Trigub, N.P.; Zamkov, V.N.; Semiatin, S.L. Mathematical modeling of aluminum evaporation during electron-beam cold-hearth melting of Ti-6Al-4V ingots. *Metall. Mater. Trans. B* **2003**, *34*, 447–454. [CrossRef]
20. Wang, J.; Peng, G.; Li, L.; Si, C.; Meng, S.; Gong, J. 30 kW-level laser welding characteristics of 5A06 aluminum alloy thick plate under subatmospheric pressure. *Opt. Laser Technol.* **2019**, *119*, 105668. [CrossRef]
21. Juechter, V.; Scharowsky, T.; Singer, R.F.; Körner, C. Processing window and evaporation phenomena for Ti–6Al–4V produced by selective electron beam melting. *Acta Mater.* **2014**, *76*, 252–258. [CrossRef]
22. Klassen, A.; Forster, V.E.; Körner, C. A multi-component evaporation model for beam melting processes. *Model. Simul. Mater. Sci. Eng.* **2016**, *25*, 25003. [CrossRef]
23. Klassen, A.; Forster, V.E.; Juechter, V.; Körner, C. Numerical simulation of multi-component evaporation during selective electron beam melting of TiAl. *J. Mater. Process. Technol.* **2017**, *247*, 280–288. [CrossRef]
24. Lütjering, G. Influence of processing on microstructure and mechanical properties of ($\alpha+\beta$) titanium alloys. *Mater. Sci. Eng. A* **1998**, *243*, 32–45. [CrossRef]
25. Kumar, C.; Das, M.; Paul, C.P.; Bindra, K.S. Characteristics of fiber laser weldments of two phases ($\alpha+\beta$) titanium alloy. *J. Manuf. Process.* **2018**, *35*, 351–359. [CrossRef]
26. Pang, S.; Hirano, K.; Fabbro, R.; Jiang, T. Explanation of penetration depth variation during laser welding under variable ambient pressure. *J. Laser Appl.* **2015**, *27*, 22007. [CrossRef]
27. Fabbro, R.; Hirano, K.; Pang, S. Analysis of the physical processes occurring during deep penetration laser welding under reduced pressure. *J. Laser Appl.* **2016**, *28*, 22427. [CrossRef]
28. Wang, J.; Hu, R.; Chen, X.; Pang, S. Modeling fluid dynamics of vapor plume in transient keyhole during vacuum electron beam welding. *Vacuum* **2018**, *157*, 277–290. [CrossRef]
29. Semak, V.; Matsunawa, A. The role of recoil pressure in energy balance during laser materials processing. *J. Phys. D Appl. Phys.* **1997**, *30*, 2541. [CrossRef]
30. Cho, W.I.; Na, S.J.; Thomy, C.; Vollertsen, F. Numerical simulation of molten pool dynamics in high power disk laser welding. *J. Mater. Process. Technol.* **2012**, *212*, 262–275. [CrossRef]
31. Huang, Y.; Hua, X.; Shen, C.; Li, F.; Ding, Y.; Mou, G. Metal evaporation flux across knudsen layer in laser keyhole welding of Al–Mg alloys with pressure balance condition method. *Appl. Surf. Sci.* **2021**, *536*, 147838. [CrossRef]
32. Han, S.-W.; Cho, W.-I.; Zhang, L.-J.; Na, S.-J. A study on laser keyhole welding in vacuum by computational fluid dynamics simulations with plume effect models. *J. Laser Appl.* **2021**, *33*, 12042. [CrossRef]
33. Luo, Y.; Tang, X.; Lu, F.; Chen, Q.; Cui, H. Effect of subatmospheric pressure on plasma plume in fiber laser welding. *J. Mater. Process. Technol.* **2015**, *215*, 219–224. [CrossRef]
34. Bykovskiy, D.P.; Petrovskii, V.N.; Uspenskiy, S.A. Investigation of the vapour-plasma plume in the welding of titanium by high-power ytterbium fibre laser radiation. *Quantum Electron.* **2015**, *45*, 218. [CrossRef]
35. Gong, J.; Peng, G.; Li, L.; Xia, H.; Meng, S.; Wang, J. Effect of plasma plume produced by vacuum laser welding on energy transmission. *Opt. Laser Technol.* **2021**, *136*, 106744. [CrossRef]